Current Applied Physics 12 (2012) 718–725

Contents lists available at SciVerse ScienceDirect

Current Applied Physics

journal homepage: www.elsevier.com/locate/cap

Effect of annealing temperature on the optical properties of nanosilicon produced from silicon monoxide

S.G. Dorofeev [a], A.A. Ischenko [b,*], N.N. Kononov [c], G.V. Fetisov [a]

[a] Department of Chemistry, Moscow Lomonosov State University, Moscow 119899, Russia
[b] Moscow Lomonosov Academy of Fine Chemical Technology, Moscow 119517, Russia
[c] Prokhorov General Physics Institute, Russian Academy of Sciences, Moscow 119991, Russia

ARTICLE INFO

Article history:
Received 9 June 2011
Accepted 14 October 2011
Available online 30 November 2011

Keywords:
Silicon nanoparticles
Spectral properties
Photoluminescence

ABSTRACT

Silicon nanoparticles (Si-NPs) capable of photoluminescence (PL) over the energy range from 790 nm to 900 nm were synthesized from silicon monoxide by increasing annealing temperatures from 25 °C to 950 °C. The PL of nanoparticles has remained stable for more than ten months from the date of the hydrosilylation of their surface by 1-octadecene. Solid samples of Si-NPs grafted with 1-octadecene are stable in the air up to 220 °C. The mean sizes of particles and their size distribution density function were derived from SAXS and XRD experiments and compared with TEM and HRTEM images and values calculated by the quantum limit model in accordance with the experimental optical absorption gap values. The absorption spectra of Si-NPs synthesized at 25 °C, 200 °C and 300 °C exhibited a blue shift of the fundamental absorption edge with respect to silicon single crystals; the absorption of Si600 and Si950 at the same incident photon shows energies increase. The PL peak of Si-NPs shifted toward longer waves as the synthesis temperature increased and exhibited a stronger red shift with respect to the photoexcitation wavelength. An analysis of the red shift led us to conclude that the surface states related to (Si–O) bonds influenced the effectiveness of PL. The Si-NPs PL quantum yield increased as the annealing temperature grew and reached a maximum of ~12% for Si-NPs at 950 °C.

1. Introduction

Silicon is one of the most technologically important materials today owing to its omnipresent significance in microelectronics. In recent decades, nanocrystalline silicon has been the focus of attention of researchers because of the effective photoluminescence (PL) of Si-NPs in the UV–VIS range. The possibility of such a PL in an indirect band semiconductor such as silicon is related to the relaxation of the momentum rule in Silicon nanoparticles (Si-NPs) less than 5 nm in diameter as a result of the quantum confinement effect.

Initially, the PL spectrum in the red region was observed for porous and nanocrystalline silicon [1–4]. Since then, the number of publications on this issue has been growing steadily. There are many ways to obtain Si-NPs, including electrochemical etching of bulk silicon wafers [5], sputtering [6], laser ablation [7,8], laser-induced pyrolysis of monosilane [9], plasma enhanced chemical vapor deposition (PECVD) [10], etc. However, the task of creating a simple and effective method for obtaining macro amounts of high-quality silicon nanoparticles capable of photoluminescence in the visible range with a high quantum yield is still of great current interest.

A promising method for Si-NPs synthesis is the isolation of nanoparticles from commercially available SiO_x ($0.4 \leq x \leq 1.6$) powders used in electronic industry. In the earliest reports on the use of SiO_x powder, Si-NPs formed in Si/SiO_2 superlattices during powder deposition on a substrate and its subsequent annealing at ~1100 °C [11,12]. However, we believe that the most efficient method for the synthesis of macro amounts of Si-NPs from SiO_x powder is its pre-heating and subsequent etching with hydrofluoric acid, as was reported in [13–15]. Minimum SiO_x powder annealing temperatures in these studies exceeded 900 °C, and it was reported [13] that, at a $SiO_{0.4}$ powder annealing temperature of 900 °C, Si-NPs photoluminescence was not detected even after etching in hydrofluoric acid. To increase PL efficiency and stability, the surface of Si-NPs was subjected to hydrosilylation. As a result, stable (Si–C) covalent bonds replaced metastable (Si–H) bonds. The hydrosilylation procedure was successfully applied in [16,17] for the passivation of the surface of Si-NPs synthesized by monosilane laser-induced pyrolysis. As a result, blue to red emitting

* Corresponding author. Tel./fax: +7 495 423 4992.
E-mail address: aischenko@yasenevo.ru (A.A. Ischenko).

1567-1739/$ – see front matter © 2011 Elsevier B.V. All rights reserved.
doi:10.1016/j.cap.2011.10.016

nanoparticles were obtained from originally non-fluorescing silicon nanoparticles. The characteristic times of thermally activated hydrosilylation were of from 3 to 48 h [14,17].

In this study, we developed a procedure for annealing SiO powders at temperatures up to 950 °C and the hydrosilylation of nanoparticles within a time range not exceeding 10 min. The mass yield of Si-NPs capable of bright red photoluminescence was 100 mg per 2 g of the initial SiO powder. The photoluminescence of nanoparticles was stable for ten months from the date of the hydrosilylation of their surface. Solid samples of Si-NPs grafted with 1-octadecene were quite stable in air up to 220 °C. The Si-NPs PL quantum yield increased as the annealing temperature grew and reached a maximum of ~12% for Si-NPs synthesized at 950 °C.

2. Experimental details

2.1. Synthesis of silicon nanoparticles

We used silicon monoxide, SiO (high purity, grade A, Reachem), hydrofluoric acid (analytical grade, Reachem), 1-octadecene (Acros, 99 + wt%), hexane (analytical grade, Ecos-1), methanol (analytical grade, Ecos-1).

Si-NPs were synthesized from silicon monoxide, SiO. The SiO powder (2 g) was ground up in an agate mortar to particle sizes of ~100 μm and heated from room temperature to 950 °C in air for 4 h in closed corundum cruicible. Si-NPs are formed in heating the prepared SiO powder from 25 °C to 950 °C according to the reaction:

$$2SiO \rightarrow SiO_2 + Si \quad (1)$$

In what follows, Si-NPs synthesized at SiO powder temperatures of 25, 200, 300, 600, and 950 °C are denoted by Si25, Si200, Si300, Si600, and Si950, respectively. The product was etched with concentrated hydrofluoric acid (HF, 49 wt%) to remove SiO_2 matrix formed after heat treatment of the initial powder. Etching was performed at 50 °C for ~20 min until cessation of gas emission ($SiF_4 + H_2$) while stirring in an ultrasonic bath with using 150 W ultrasound power, frequency $\nu = 37$ kHz (PULSE 270 M-002935). After etching in HF a suspension of nanoparticle agglomerates is obtained. The suspension was diluted with water 10 times and centrifuged. Centrifugate (supernatant fluid) is separated, and the sediment with water and muddle was again mixed by ultrasound for 1 min and then centrifuged. Centrifugate is separated, and the sediment covered with methanol (in this case stood out gas; separate checks during prolonged treatment with methanol for 2 h revealed no spectral differences) and muddle on ultrasound 1 min. Centrifugate is again separated. Centrifugations were done using: 2000× *g*, for 20 min. Distilled water was used in every instance where water was used.

2.2. The protection of nanosilicon particles with alkenes

The procedure for the temperature-initiated hydrosilylation of silicon nanoparticles saturated with (Si–H) bonds is described in [16,17]. It is based on the observation that, at high temperatures, some (Si–H) bonds dissociate, Si–H → Si· + H·. Further, some silicon dangling bonds can interact with alkenes having terminal double bonds:

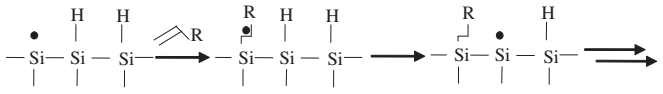

We used 1-octadecene as organic molecules with terminal double bonds. Silicon nanoparticles collected after centrifugation were dispersed in a quartz tube in a solution of toluene (4 ml). The suspension was subjected to ultrasonic mixing, and 1-octadecene (4 ml) was then added to it. The test tube was heated to the 1-octadecene boiling point (315 °C) and held at this temperature for 5 min. 1-octadecene boiling provides intense mixing of initially insoluble particles. This temperature-activated hydrosilylation procedure differed from a similar procedure described in Refs. [14,17] by a higher temperature, at which hydrosilylation was performed, and resulted in a significantly shorter time during which the process was conducted. At the end of a 5-min hydrosilylation interval, initially turbid solution became transparent and turned reddish-brown. After Si-NPs hydrosilylation, the mixture was cooled, diluted with hexane 3 times, and then centrifuged. The precipitate was separated, and the centrifugate containing nanoparticles in solution was mixed with methanol (1:1) for coagulation and again centrifuged. The centrifugate is separated, the precipitate was dissolved in hexane without ultrasound to obtain nanoparticles in solution. For further purification it was mixed with methanol (1:1) for coagulation of the sol and again centrifuged. Centrifugate was separated, and the precipitate was dissolved in hexane (toluene or chloroform) to give purified nanoparticles in sol. With all these solvents, Si-NPs formed stable sol. Hydrosilylation caused a significant increase in the intensity of photoluminescence than that which was observed immediately after SiO powder etching with concentrated hydrofluoric acid. Hydrosilylized Si-NPs samples were studied using a LEO 912 AB OMEGA and Jeol-JEM 2100 F/Cs transmission electron microscope at an accelerating voltage of 200 keV. The transmission spectra were recorded with Avantes-AVA-Spec-2048 and SF-104 (Interphotophyisics) spectrophotometers over the range 200–1000 nm. The photoluminescence of Si-NPs was excited by diode lasers with wavelengths of 407 and 532 nm and light-emitting diodes (LED) with a maximum intensity near 405 nm. The photoluminescence spectra were recorded using an Avantes-AVA-Spec-2048 spectrophotometer.

In the present study, we developed a procedure for annealing SiO powders at temperatures up to 950 °C and the hydrosilylation nanoparticles within a time not exceeding 10 min. The mass yield of Si-NPs capable of bright red photoluminescence was 100 mg per 2 g of the initial SiO powder (~16% of theoretical yield). The photoluminescence of nanoparticles was stable for ten months from the date of the hydrosilylation of their surface.

2.3. Structural properties

The structures of the synthesized Si-NPs were studied by TEM and HRTEM. A typical TEM and HRTEM photomicrograph of Si-NPs is shown in Fig. 1. An analysis of images showed that the maximum size of particles in all the samples did not exceed 4 nm. The inset in Fig. 1 also shows a selected area electron diffraction pattern obtained for Si-NPs. To improve the picture of diffraction rings, the inset consists of two micrographs obtained using different exposure times. The diffraction rings from Si-NPs were identified with silicon atomic planes by comparing their diameter with that of gold foil rings (gold was used as an internal reference). As a result, the Si-NPs interplanar distances were identified and the corresponding Miller indices were determined. An analysis shows that the diffraction rings nearest to the center (Fig. 1) correspond to the silicon (111), (220), (311), and (331) atomic planes.

The crystallinity of the particles was also confirmed by X-ray powder diffraction (XRD) experiments carried out on the sample obtained at temperature 200 °C. The XRD measurements were performed in a high resolution imaging-plate (IP) Guinier camera Huber G670 [18] with Cu $K\alpha_1$ radiation ($\lambda = 1.5405981$ Å) from a sealed X-ray tube operated at 30 kV, 40 mA. The data recording from the sample in the form of the powder adhered to a thin flat

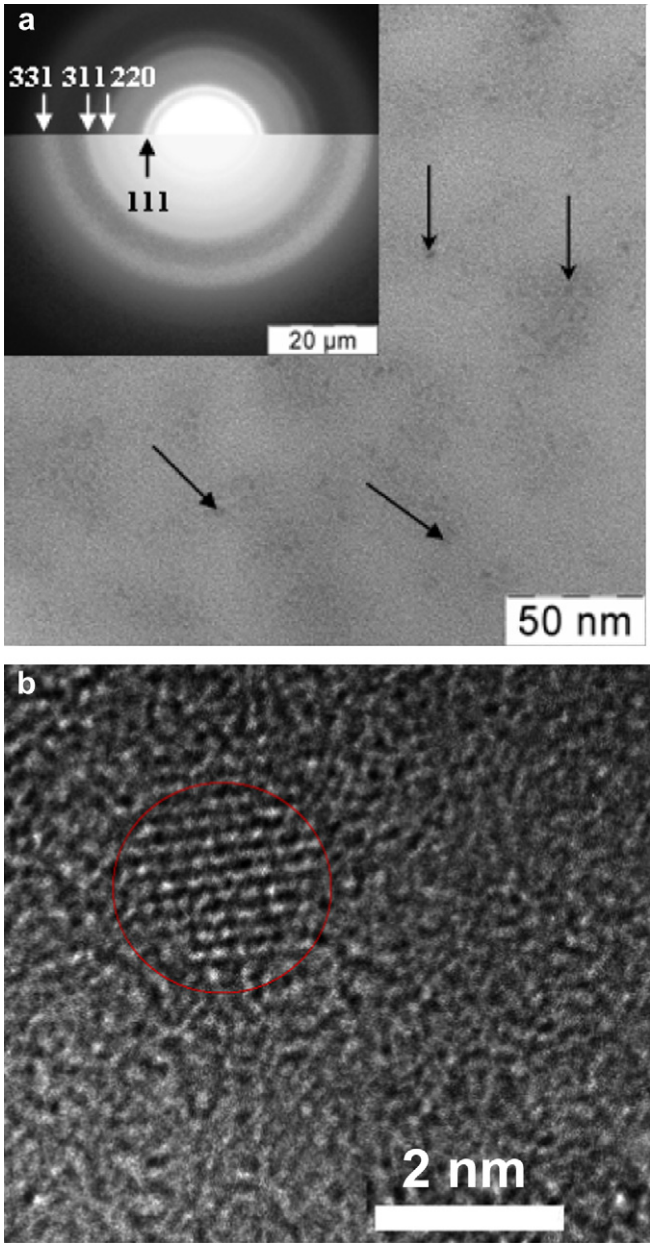

Fig. 1. Si-NPs TEM images. (a) The inset shows a selected electron diffraction pattern area for Si-NPs sample synthesized at 300 °C (Si300 sample). LEO 912 AB OMEGA; accelerating voltage of 200 keV (b) HRTEM, Jeol-JEM 2100 F/Cs, accelerating voltage of 200 keV. Red circle pointed single silicon nanoparticle. (For interpretation of the references to colour in this figure legend, the reader is referred to the web version of this article.)

polymeric foil (6 μm thick Mylar) attached to the sample holder in transmission-asymmetric geometry was made by a flexible IP detector bent according to camera radius 90 mm and covering the scattering angles 2θ from 1° to 100°. The XRD pattern of the sample together with a pattern of the standard crystalline Si powder having average grain diameter about 0.2 μm is shown in Fig. 2. The narrow Bragg peaks of the standard crystalline Si powder exactly correspond to FCC Brave unit cell with the lattice parameter 0.54311 nm (diamond structure, space group $Fd\bar{3}m$). The maxima of three clearly observed peaks on the XRD pattern of Si200 sample match to those of the standard crystalline powder having indices *hkl* 111, 220 и 311, that proves the sample crystallinity.

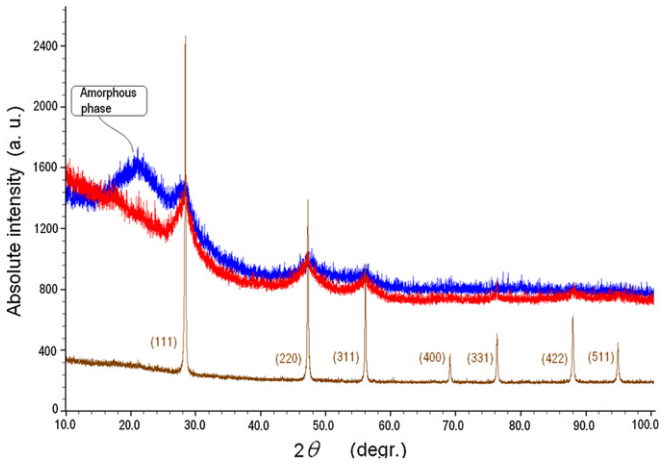

Fig. 2. X-ray powder diffraction patterns demonstrating the crystallinity of the particles in sample Si200. *Brown line* – XRD pattern of the standard crystalline Si (*hkl* indices are shown near the Bragg peaks). *Blue line* - XRD pattern of the synthesis product obtained at 200 °C before atching in HF. *Red line* – the same product after etching in HF (sample Si200). Etching removed the amorphous phase and revealed the footprints of high angle peaks (331), (422) and (511) of c-Si. The data were collected during 14 h compared to 30 min for the standard c-Si. (For interpretation of the references to colour in this figure legend, the reader is referred to the web version of this article.)

The weaker Bragg peaks 400 and 331 of silicon are not observed in Si200 pattern because of shading by a high background from the polymer substrate, due to the volume of the probe material available for the analysis not being sufficient to completely cover the irradiated area of the substrate (12×20 mm^2). The large breadth (more than 2° in 2θ) of the observed peaks on Si200 XRD pattern is due to very small crystalline domains.

The poor quality of the XRD pattern does not allow for a crystal size determination by means of modern full profile analyses [19]. Simple estimates of the spherical crystalline domain sizes according to the Scherrer formula and average deformations according to Wilson formula based on peak profile width taking into account the instrumental function [19] gave us the value of 2.5 nm for the average crystalline particle diameter at mean relative deformation 0.8%. However, one should be cautious with such estimates as far as these early theories do not allow for crystal lattice breaking at short distances like it is in the case of nanoparticles substantially smaller than 10 nm.

More correct nanoparticle size determinations may be done by the small angle X-ray scattering technique (SAXS) using the principles described in details e.g. in monographs [20,21]. SAXS measurements were performed with a high flux SAXS instrument (SAXSess, Anton Paar) equipped with Göbel mirror and Kratky block-collimation system [22] using Cu Kα radiation from a line focus of a sealed X-ray tube. Samples in the form of a solution of particles in hexane were placed into a special Anton Paar's quartz capillary sample holder. The scattering patterns were recorded on an imaging plate (IP) detector in the diffraction angle 2θ range 0°–30°. The 2D pattern from the IP was integrated and transformed to 1D intensity distribution $I(q)$ with the aid of SAXSQuant 2.0 software (Anton Paar, GmbH). The SAXS part in the range of scattering vector $0.08 < q < 2.00$ nm^{-1} was processed for particle size determination. After the subtraction of the background scattered by the capillary and solvent, data desmearing (X-ray tube focus length deconvolution) was performed. Particle size distribution density functions $p(r)$ were computed from the desmeared SAXS data using the generalized indirect Fourier transformation with the aid of GIFT program [23,24] in the approximation of a polydispersed spherical particle system. The results for all the investigated samples are shown in Fig. 3.

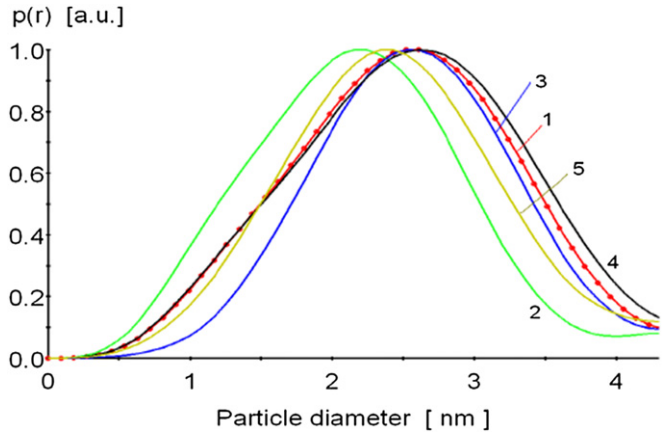

Fig. 3. Particle size distributions derived from the SAXS data. Curves 1–5 relate to the Si-NPs samples synthesized at temperatures 25, 200, 300, 600 and 950 °C respectively. For better comparison of curve positions and widths, the graphs have been reduced to unit heights, therefore their shapes differ from lognormal size density distribution really observed in the samples. The values of particle diameters D_{mode} corresponding to the main maxima of the curves are given in Table 1.

2.4. Thermogravimetric analysis

The differential scanning calorimetry (DSC) and thermogravimetric analysis (DTG) (NETZSCH STA 409 PC/PG) of preliminarily dried 1-octadecene grafted silicon particles (120 °C) was carried out using a heating rate of 5 °C/min from 20 to 400 °C. Sample mass was 6 mg, Al_2O_3 crucible. A small weight loss over the temperature range 170–220 °C is most likely related to the removal of residual solvent (hexane: nanoparticles were isolated from a hexane solution) present in the octadecene coat. Above 220 °C, intense weight loss begins. It is accompanied by a substantial endothermic effect likely caused by the decomposition of the octadecene coat. The conclusion can be drawn that the nanoparticle samples studied are quite stable in air up to 220 °C.

2.5. Spectroscopic characterization

Infrared spectra were recorded on Specord-M82 spectrometer with a typical spectral resolution of 2 cm^{-1}. The spectra (Fig. 4) show that the functionalization of Si-NPs with 1-octadecene yields alkyl-terminated nanoparticles. Spectra exhibit three close-lying absorption bands centered at 2904 cm^{-1} and being characteristic for $\nu(C-H_x)$ stretching modes. At the same time, physosorption of free alkenes with characteristic bands $\nu(C{=}C) \sim 1650\ cm^{-1}$ or $\nu(C{=}CH_2) \sim 3050\ cm^{-1}$ is not observed.

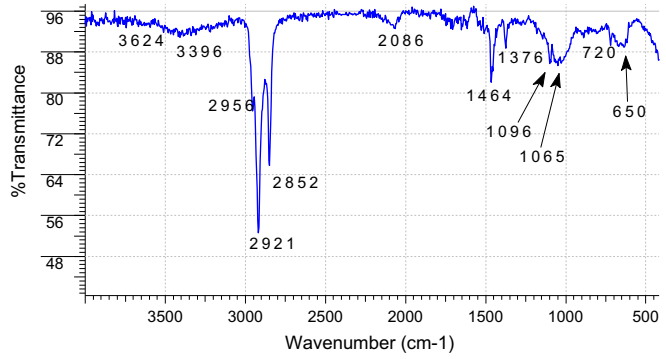

Fig. 4. Infrared spectrum of silicon nanoparticles produced at 950 °C (Si950) and hydrosilylated with 1-octadecene.

The data correspond to 1-octadecene terminated samples prepared through thermal hydrosilylation treatment: $\nu_{as}(C-H$ in $CH_3) = 2956\ cm^{-1}$; $\nu_{as}(C-H$ in $-CH_2-) = 2921\ cm^{-1}$; $\nu_s(C-H$ in $-CH_2-) = 2852\ cm^{-1}$; $\nu[(Si_3)Si-H] = 2086\ cm^{-1}$; scissoring vibration $\delta(CH_2) = 1464\ cm^{-1}$; umbrella type of vibration, $\delta_s(CH_3) = 1376\ cm^{-1}$. Oxidation could be a concurrent reaction to hydrosilsilylation and vibrational modes $\nu_{as}(Si-O) = 1096\ cm^{-1}$, $\nu_s(Si-O) = 1065\ cm^{-1}$ can be assigned to (−O−Si−O−) bonds on the Si-NPs surface; absorption bands at 3624 cm^{-1} and 3396 cm^{-1} are characteristic for stretching vibrations of (O−H) groups [25,26]. The small peak at 720 cm^{-1} can be assigned to rocking vibration of ($-CH_2-$) groups, $r(-CH_2-)$. The vibrational stretching mode for Si−C is seen, $\nu(Si-C) = 650\ cm^{-1}$, in accordance with earlier observations of [25]. The broad peak at 650 cm^{-1} can be assigned to the formation of Si−C bonds, and provides a direct proof that the reaction was successful. The absorption intensity of $\nu[(Si_3)Si-H]$ stretching mode at 2086 cm^{-1} can be used as a relative index of hydrosilylation reaction progress. The integral intensity ratio $I(\nu_{as}(C-H)/I[(Si_3)Si-H] \sim 13$ of $\nu_{as}(C-H$ in $-CH_2-) = 2921\ cm^{-1}$ and $\nu[(Si_3)Si-H] = 2086\ cm^{-1}$ indicate the high power of completeness the hydrosilylation process [25]. Similar spectra have been reported in the literature for other hydrosilylated silicon nanoparticles (see, e.g. review article [26]).

3. Results and discussion

3.1. Absorption spectra

Transmission spectra of silicon nanoparticles, dispersed in hexane were recorded in the range from 300 nm up to 1100 nm for samples Si25, Si200, Si300, Si600 and Si950. Transmittance of silicon nanoparticles was determined as the ratio of intensity of probing radiation transmitted through quartz cell with hexane containing Si-NPs to that transmitted through the same cell with pure hexane. For further calculation of Si-NPs absorption coefficient, the reflection spectra were measured by similar technique. The Si-NPs absorption coefficient α was calculated from the equation [27]:

$$T = \frac{(1-R)^2 e^{-\alpha d}}{1 - R^2 e^{-2\alpha d}} \tag{2}$$

Equation (2) determines passage of radiation through the absorbing layer at multiple reflections of this radiation from boundaries of a layer. T and R are the measured normalized transmittance and reflectance of silicon nanoparticles; d is the effective thickness of Si-NPs layer along a propagation direction of the probing radiation. Scattering of probing radiation on solutions with silicon nanoparticles was insignificant and we neglected this process in our calculations.

The concentration of Si-NPs in all the studied solutions was identical and equal to $C = 75$ μg/ml. To calculate the Si-NPs effective absorption length in solutions, we have used the fact that the maximum Si-NP sizes do not exceed 5 nm. Hence, at a concentration of 75 μg/ml the number density of silicon nanoparticles in solutions under investigations turn out $\sim 5.5 \times 10^{14}\ cm^{-3}$. Accordingly, at this concentration the average distance between adjacent nanoparticles is ~120 nm. Therefore, when calculating the Si-NPs absorption coefficient in the wavelength range from 300 nm up to 1100 nm in colloidal solution with discretely located therein nanoparticles can be regarded as a continuous medium with an effective thickness is determined by the following formula:

$$d = \frac{C \cdot L}{\rho} \tag{3}$$

Here, ρ equals mass density of Si-NPs and L equals the thickness of cell in a direction parallel to the propagation direction of the probe radiation, which in our experiments was 1 cm.

Absorption coefficients calculated for Si-NPs synthesized at elevated temperatures (Si25, Si200, Si300, Si600 and Si950 samples) are shown in Fig. 5. The same figure shows the absorption spectra of silicon single crystals (c-Si) for comparison.

Fig. 5 shows that, near the silicon fundamental absorption edge, samples Si25, Si200 and Si300 exhibit blue shifts with respect to the absorption by c-Si. However, whereas the absorption behavior of Si25, Si200, Si300 nanoparticles at incident photon energies of ~1.25 eV is similar to the absorption spectrum of silicon single crystals, the absorption of Si600 and Si950 at the same incident photon shows energies increase. For microcrystalline and amorphous silicon, increased absorption is usually associated with structural defects [28,29]. It can therefore be suggested that the concentration of defects in silicon nanoparticles synthesized at temperatures 600 °C and 950 °C is significantly higher than in the nanoparticles formed at lower temperatures. In Fig. 6, the absorption spectra are shown in the coordinates $\sqrt{\alpha \cdot h\nu} - h\nu$, where α is the sample absorption coefficient for photons with the energy $h\nu$. Fig. 6 shows the energy area for all the analyzed curves, where the plots are well approximated by the linear function:

$$\sqrt{\alpha \cdot h\nu} = A(h\nu - E_g) \tag{4}$$

In equation (4), A depends on the matrix element of optical transition and convolution valence and conduction bands energy [30]. Graphically, the E_g value is defined as the intersection of linear approximation (equation (4)) with the $h\nu$ axis.

For samples Si25, Si200, Si300, Si600 and Si950, E_g values are 2.60, 2.55, 2.50, 2.30 and 2.50 eV respectively. The dependence of equation (4) is characteristic of indirect transitions near the crystalline and amorphous silicon fundamental absorption edge [31,32]. Accordingly, the E_g value determines the width of the fundamental gap $\Gamma'_{25} - X_1$. In this case, such a dependence is valid in the energy range $2.6 \leq h\nu \leq 3.6$ (eV), i.e. far from the fundamental absorption edge of the silicon single crystal. However, in [33,34], dependence (4) was observed near the $\Gamma'_{25} - L_1$ indirect transition of p-Si and Si-NPs. Accordingly, we believe that the measured E_g values 2.60; 2.55; 2.50; 2.30 and 2.50 eV correspond to the width of the Si-NPs band gap for the $\Gamma'_{25} - L_1$ indirect transition. For c-Si at room temperature, $E_g(\Gamma'_{25} - L_1) \equiv E_g(\text{c-Si}) = 1.8$ eV [35]. Consequently, for nanoparticles in samples Si25, Si200, Si300, Si600, and Si950, the $E_g(\Gamma'_{25} - L_1)$ value is larger than E_g(c-Si) by 0.80, 0.75, 0.70, 0.50, and 0.70 eV, respectively. Note that the absorption spectra measured for each sample are associated with ensembles of Si-NPs with different mean nanoparticles sizes, as follows from the SAXS data (Fig. 3). Therefore, the calculated band gap energies are ensemble averages for the corresponding sample.

3.2. Si-NPs photoluminescence

All the recorded photoluminescence spectra (Avantes - AVASpec-2048) were corrected taking into account the spectral instrumental function.

For the spectrometer spectral function characterization, radiation produced by a tungsten filament heated to a temperature of 2400 °C was recorded. The spectrum was then compared with the spectrum of blackbody radiation of the same temperature corrected by the tungsten blackness factor. The spectrometer spectral function was obtained through dividing the theoretical tungsten emission spectrum by the recorded spectrum. The photoluminescence spectra excited in Si-NPs samples Si25, Si200, Si300, Si600, and Si950 at a wavelength of 405 nm are shown in Fig. 7. As we can see from Fig. 7, the spectra of all the samples are strongly structured.

To determine the spectral composition of the photoluminescence peak, the signal was approximated by four Lorentzian contours. A typical example of such an approximation for sample Si950 is shown in Fig. 8.

The position of each experimental peak on the wavelength axis was calculated as a weighted average of the positions of the Lorentzian contours with weights corresponding to the integrated intensity in each profile. The photoluminescence peak E_{PL} are listed in Table 1 as depending on sample synthesis temperatures. Table 1 also contains Si-NPs band gaps $E_g(\Gamma'_{25} - L_1)$ calculated from the absorption spectra and the Stokes shifts, which were determined as the differences between the energy gap E_g and the photon energy E_{PL} at the photoluminescence peak maximum. Table 1 also presents the average diameters of Si-NPs calculated by the quantum limit

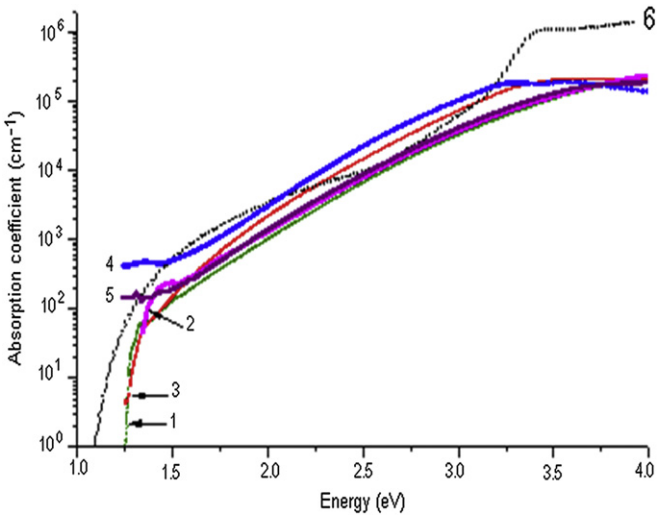

Fig. 5. Absorption spectra of Si-NPs synthesized from SiO powder at elevated temperatures from 25 °C to 950 °C (samples Si25 -1, Si200 – 2, Si300 – 3, Si600 - 4 and Si950 – 5). As a reference, spectral dependence of crystalline silicon absorption is shown by curve 6.

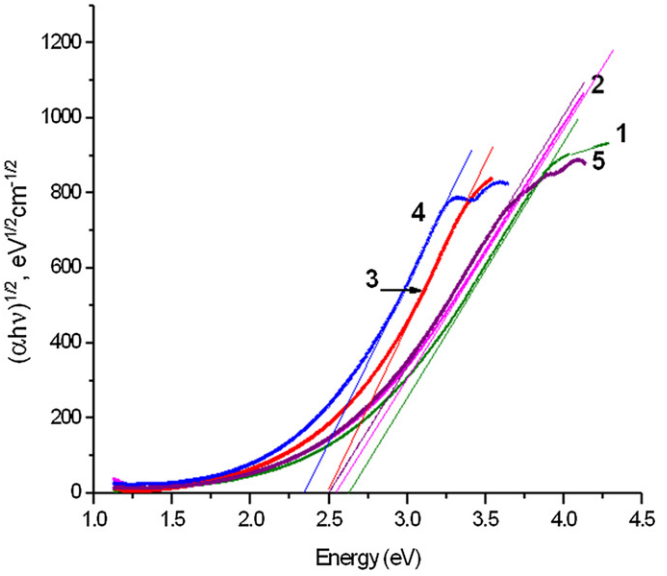

Fig. 6. Si-NPs absorption spectra from SiO powder at elevated temperatures from 25 °C to 950 °C (samples Si25 -1, Si200 – 2, Si300 - 3, Si600 - 4 and Si950 - 5).

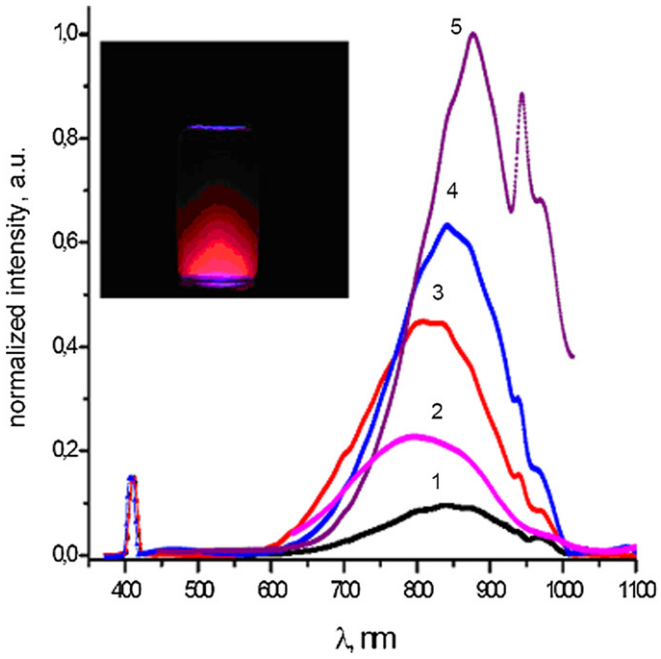

Fig. 7. Si-NPs photoluminescence spectra. Numbers 1-5 correspond to samples Si25, Si200, Si300, Si600, and Si950, respectively. Excitation wavelength is 405 nm. The inset shows a photograph of Si-NPs photoluminescence for Si300.

model [36,37] in accordance with the experimental E_g values. The calculated values are in agreement with the experimental data derived from SAXS measurements (Fig. 3).

Table 1 shows that the E_g values monotonically decrease for samples Si25, Si200, Si300 and Si600, whereas there is a noticeable increase in the band gap for sample Si950. In accordance with the E_g values, the average Si-NPs diameter in the ensembles increases to 2.5 nm, and then, in the Si950 sample, decreases to 2.1 nm. Simultaneously, the E_{PL} value decreases monotonically as the synthesis temperature grows, which corresponds to a shift of the PL toward longer wavelengths, regardless of the Si-NPs average diameter. Accordingly, the Stokes shift first decreases, reaches a minimum of 0.85 eV for sample Si600, and then increases to 1.12 eV for Si950. A large Stokes shift indicates that photorecombination is not via free

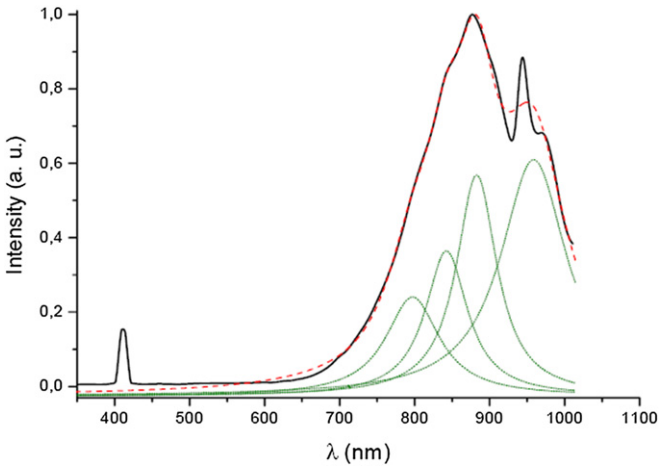

Fig. 8. Si-NPs photoluminescence spectra (Si950 sample). The black solid line is the experimental spectrum; the red line is the approximation with four Lorentzian contours (shown by dark green lines). (For interpretation of the references to colour in this figure legend, the reader is referred to the web version of this article.)

Table 1
Optical characteristics and average Si-NPs diameters depending on synthesis temperature.

Temperature, °C	25	200	300	600	950
Optical absorption gap[a], eV	2.60	2.55	2.50	2.33	2.50
Si-NPs average diameter[b], nm	2.0	2.0	2.1	2.5	2.1
Si-NPs SAXS[c] D_{mode}, nm	2.6	2.2	2.5	2.6	2.4
PL peak energy maximum, eV	1.57	1.53	1.52	1.48	1.38
Stokes shift, eV	1.03	1.02	0.98	0.85	1.12

[a] Estimated average uncertainties are 0.02 eV.
[b] Calculated by the quantum limit model [36,37] in accordance with the experimental E_g values.
[c] The values of particle diameters D_{mode} corresponding to the main maxima of the curves (Fig. 3). Average uncertainties in D_{mode} values are 0.2 nm.

exciton states, but via some impurity energy levels in the band gap of Si-NPs.

The problem of a large photoluminescence red shift, which is observed in the visible spectrum of silicon nanoparticles, was studied in [38–40]. These studies reveal that the most likely source of localized levels in the band gap of a nanoparticle less than 3 nm in diameter is oxygen atoms situated on the surface and connected to silicon with the formation of (Si–O) bonds. These studies also demonstrated that the red shift of photoluminescence could reach ~1 eV. As noted above, the surface of Si-NPs was passivated by 1-octadecene molecules. As a result, surface dangling bonds should be saturated with carbon atoms that formed (Si–C) bonds. If we assume that the Stokes shift is determined by the presence of oxygen atoms on the surface, then it indicates that certain number of oxygen atoms cover the surface of nanoparticles. The E_{PL} values for Si600 and Si950 are 1.48 and 1.38 eV, respectively. However, it follows from the absorption spectra shown in Fig. 5 that, at incident photon energies $1.0 \leq h\nu \leq 1.8$ eV, the absorption behavior of these samples differs significantly from that of the Si25, Si200 and Si300 samples. We attribute this difference to a higher concentration of defects in Si600 and Si950, which determine the main absorption in this range. We believe that the main source of these defect states in the Si-NPs band gap is dangling bonds on the surface of nanoparticles, i.e., covalent bonds of silicon atoms not saturated with hydrogen and oxygen atoms or (Si–O) bonds. Thus, in Si600 and Si950, the photoexcited exciton recombination of an electron – hole pair is accomplished not only through the settlement of radiation levels determined by bonds of the (Si–O) fragments, but also as a result of collisional recombination via defect levels associated with dangling bonds of silicon atoms arranged on the surface of Si-NPs. This effect should in principle decrease the efficiency of photoluminescence in the samples under study.

The Si-NPs photoluminescence quantum yield in hexane was measured by comparing the photoluminescence signals of Si-NPs and rhodamine 6G dissolved in ethanol. It is known that the rhodamine 6G quantum yield at a 0.08 optical density at the photoexcitation wavelength ($337 \leq \lambda_{ex} \leq 530$ nm) is 85%. For comparison, the photoluminescence Si-NPs sol and rhodamine 6G were prepared so that their optical densities were identical and were 0.08 at wavelength $\lambda = 405$ nm. We measured the total areas under the peaks of Si-NPs and rhodamine 6G photoluminescence, and, from a comparison of these areas, calculated the quantum yield of the samples. Fig. 9 shows the dependence of the Si-NPs quantum yield on the synthesis temperature.

It follows from Fig. 9 that the quantum yield increases from 0.3 % to 11.7 % as the temperature of synthesis grows from 25 °C to 950 °C. Increasing the annealing temperature leads to an increase in the concentration of luminescent centers associated with the inclusion of oxygen in the silicon nanoparticles [41].

For Si300, the quantum yield was measured at two photoexcitation wavelengths, $\lambda_1 = 405$ nm (photon energy 3.06 eV) and

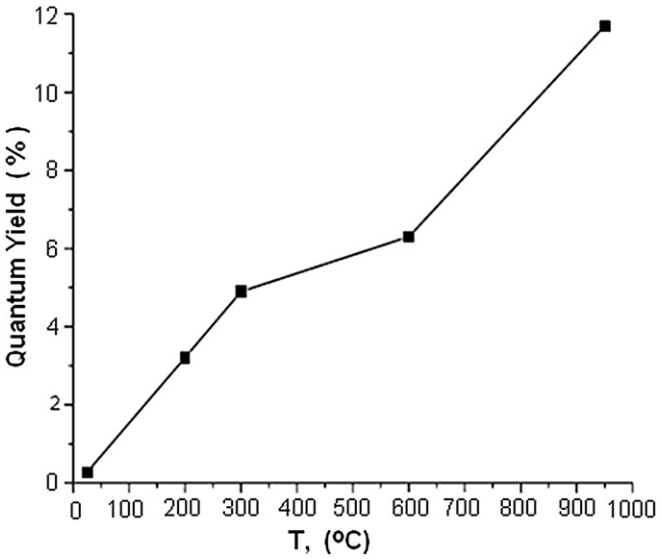

Fig. 9. Dependence of the Si-NPs quantum yield (QY) on the annealing temperature.

λ_2 = 532 nm (photon energy 2.33 eV). Radiation power was P_1 = 30 mW and P_2 = 100 mW, respectively. The photoluminescence spectra excited by these radiation sources are shown in Fig. 10. As is seen from Fig. 10, the shape of the PL signal is almost independent of wavelength and exciting radiation power.

The ratio between the quantum yields of photoluminescence excited at wavelengths λ_1 and λ_2 is determined by the equation:

$$\frac{\eta_2}{\eta_1} = \frac{I_{Ph2} I_1 \lambda_1 (1 - e^{-D_1})}{I_{Ph1} I_2 \lambda_2 (1 - e^{-D_2})} \quad (5)$$

Here I_{Ph1} and I_{Ph2} are the integral photoluminescence energy spectra (area under the respective peaks) recalculated to the number of photons when excited by radiation with wavelengths λ_1 and λ_2. I_1 and I_2 are the intensities of incident pumping radiation, and D_1 and D_2 are the optical densities of the sample at the wavelengths λ_1 and λ_2. Using this equation and the corresponding

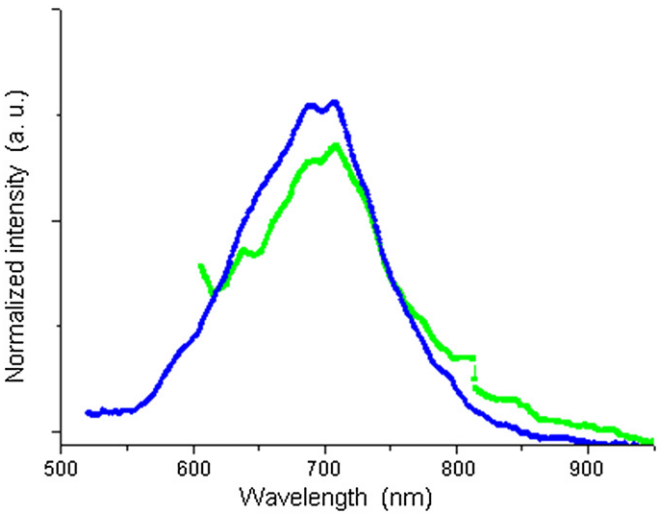

Fig. 10. Si-NPs photoluminescence spectra (sample Si300). Quantum yield was measured at two photoexcitation wavelengths, λ_1 = 405 nm (blue, photon energy 3.06 eV) and λ_2 = 532 nm (green, photon energy 2.33 eV); radiation power P_1 = 30 mW and P_2 = 100 mW, respectively. (For interpretation of the references to colour in this figure legend, the reader is referred to the web version of this article.)

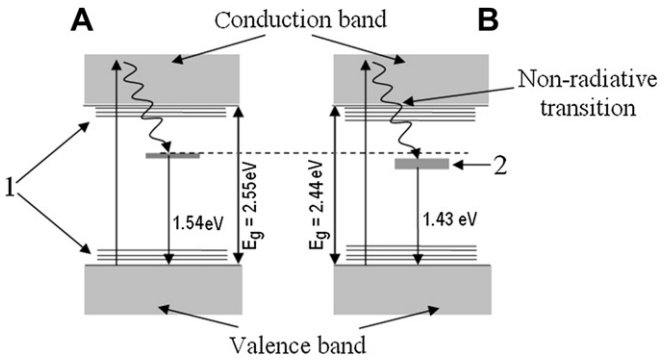

Fig. 11. Schematic diagram of Si-NPs energy levels, synthesized at 25 °C, 200 °C and 300 °C temperatures (A); 600 °C and 950 °C - (B). 1 - energy levels determined by the surface states of Si-NPs. 2- energy levels due to (Si–O) bonds. Eg = 2.55 eV and 2.44 eV correspond to average values for Si25, Si200, Si300 (A) and Si600, Si950 samples (B) respectively; E = 1.54 eV and 1.43 eV refer to PL peak energy maximum for Si25, Si200, Si300 (A) and Si600, Si950 samples (B) respectively (see Table 1).

D_1 and D_2 values determined from the absorption spectrum of Si-NPs (Si300 sample) gave the ratio of quantum yields: η_2/η_1 = 0.92. Thus, when photoluminescence is excited by photons with energies of 3.06 eV and 2.33 eV, the quantum yields are approximately equal. Since the 2.33 eV photon energy is close to the band gap of the Si300 ensemble (determined from optical absorption, Table 1), it follows from this equality that: (i) The energy loss of photoexcited nanoparticles at the stage of relaxation from the highest state of excitation by 3.06 eV photons to the state determined by a (Si–O) bond is very small. (ii) The main energy loss leading to a decrease in the photoluminescence quantum yield is related to collisional recombination via defect levels lying below the (Si–O) level.

As can be seen from the estimates based on the analysis of the absorption spectra (Figs. 5 and 6) and SAXS measurements (Fig. 3), the mean Si-NPs size synthesized at different annealing temperatures of silicon monoxide are independent of the synthesis temperature in the estimated uncertainty limits (Table 1). Accordingly, the average band gap values of the nanoparticles do not depend on the annealing temperature. However, with increasing annealing temperature, photoluminescence spectra of the synthesized nanoparticles exhibit a red shift and the quantum yield of photoluminescence increases (Fig. 9). Nature of this phenomenon can be rationalized if we consider observed independence of the quantum yield for each sample Si25–Si950 on excitation wavelength in the range of 400–530 nm, corresponding to a photon energy 3.1–2.3 eV (Fig. 10). This observation implies that the population of the upper emitting level in Si-NPs occurs by collisions without significant loss of energy. As already noted, the upper emitting levels in the studied silicon nanoparticles are in the band gap of silicon nanoparticles, and very likely related to the (Si–O) bonds [38,42–45].

Under this assumption, increasing the red shift of the photoluminescence spectrum of nanoparticles should denote a decrease in the (Si–O) levels with respect to the band gap of silicon nanoparticles (see Fig. 11). It is also likely that the increase in annealing temperature leads to a higher density of states associated with the (Si–O) bonds [41,46].

4. Conclusions

Silicon nanoparticles capable of photoluminescence in the visible range were synthesized from silicon suboxide powder (SiOx, $x \approx 1$) heated at temperatures from 25 °C to 950 °C and then etched

with concentrated hydrofluoric acid. Etching removed the amorphous phase and revealed the XRD footprints of high angle peaks (331), (422) and (511) of c-Si (Fig. 2). Earlier it was observed the significant improvements in the PL quantum yield during the acid treatment, suggesting improvement in dangling bond passivation [45]. Hydrosilylation procedure was used to attach 1-octadecene molecules to Si-NPs surface. As a result, Si-NPs photoluminescence brightness increased substantially and became stable in time. The photoluminescence of nanoparticles was stable for more than ten months from the date of the hydrosilylation of their surface. Solid samples of Si-NPs grafted with 1-octane are quite stable in air up to 220 °C.

The absorption spectra of Si-NPs synthesized at 25 °C, 200 °C and 300 °C by heating SiO powders exhibit a blue shift of the fundamental absorption edge compared with silicon single crystals. The blue shift value is inversely proportional to the annealing temperature of SiO powders. An analysis of the absorption spectra showed that the band gap in the ensembles of Si-NPs formed by heating SiO powders decreased from 2.60 to 2.30 eV as the temperature of heating increased from 25 °C to 600 °C and increased to 2.50 eV as the temperature increased to 950 °C.

The concentration of defects in Si-NPs synthesized at temperatures 600 °C and 950 °C was significantly larger than in the nanoparticles, synthesized at lower temperatures, and the Si-NPs photoluminescence peak shifted toward longer wavelengths as the synthesis temperature increased. It follows from an analysis of the photoluminescence spectrum excited by photons with energies lower than the $\Gamma'_{25} - \Gamma_{15}$ silicon direct band gap width that the PL signal broadened and shifted monotonically to longer wavelengths as the temperature of Si-NPs synthesis increased. The Stokes shift and optical absorption gap first decreased, reached a value of 0.85 eV at a 600 °C annealing temperature, and then increased to 1.12 eV at the highest annealing temperature equal to 950 °C. The PL quantum yield and red shift increased monotonically from 0.25 % to 11.7 % as the temperature of annealing grew. Equal QY of photoluminescence excited by photons with energies larger than or about the Si-NPs indirect band gap width suggest that the major energy loss leading to a decrease in QY is related to the collisional deactivation of Si-NPs photoexcited levels through states associated with surface defects. An analysis of the red shift led us to conclude that the surface states related to (Si—O) bonds influenced the effectiveness of PL. The Si-NPs PL quantum yield increased as the annealing temperature grew and reached a maximum of ~12% for Si-NPs at 950 °C.

Acknowledgements

This work was financially supported by the Russian Foundation for Basic Research, project 09-02-12325-ofi_m and 10-02-92000—NNS_a (RP10E03). The authors thank V.B Laptev and E.A. Ryabov (Institute of Spectroscopy RAS, Moscow, RF), V.N. Bagratashvili (IPLIT RAS, Moscow, RF), A.V. Bakhtin (MITHT, Moscow, RF), J. Beckman (Therapon, Springdale, AR, U.S.A) and V. Vostrikov (University of Arkansas, U.S.A).

References

[1] L.T. Canham, Applied Physics Letters 57 (1990) 1046–1048.
[2] H. Takagi, H. Ogawa, A. Yamazaki, A. Ishizaky, T. Nakagiri, Applied Physics Letters 56 (1990) 2379–2380.
[3] Y. Kanemitsu, T. Ogawa, K. Shiraishi, K. Takeda, Physical Review B 48 (1993) 4883–4886.
[4] W.L. Wilson, P.F. Szajowski, L.E. Brus, Science 262 (1993) 1242–1244.
[5] Z. Yamani, W.H. Thomson, L. Abuhassan, M.N. Nayfeh, Applied Physics Letters 70 (1997) 3404–3406.
[6] M. Dofrat, Y. Goshen, J. Jedrzejewski, I. Balberg, A. Sa'ar, Physical Review B 69 (1–8) (2004) 155311.
[7] A. Seraphin, S.T. Ngiam, K.D. Kolmbrander, Journal Applied Physics 80 (1996) 6429–6433.
[8] V. Narayanan, R.K. Thareja, Modern Physics Letters B 17 (2003) 121–129.
[9] X. Li, Y. He, S.S. Talukdar, M.T. Swihart, Langmuir 19 (2003) 8490–8496.
[10] J. Barreto, M. Perálvarez, J.A. Rodríguez, A. Morales, M. Riera, M. López, B. Garrido, L. Lechuga, C. Dominguez, Physica E 38 (2007) 193–196.
[11] Z.H. Lu, D.J. Lockwood, J.M. Baribean, Nature (London) 378 (1995) 258–260.
[12] M. Zacharias, J. Heitmann, R. Scholz, U. Kahler, M. Schmidt, J. Bläsing, Journal Applied Physics Letters 80 (2002) 661–663.
[13] S.M. Liu, S. Sato, K. Kimura, Langmuir 21 (2005) 6324–6329.
[14] S.M. Liu, Y. Yang, S. Sato, K. Kimura, Chemical Materials 18 (2006) 637–642.
[15] S. Sato, M.T. Swihart, Chemical Materials 18 (2006) 4083–4088.
[16] X. Li, Y. He, M.T. Swihart, Langmuir 20 (2004) 4720–4727.
[17] F. Hua, M.T. Swihart, E. Ruckenstein, Langmuir 21 (2005) 6054–6062.
[18] J. Gal, D. Mogilanski, M. Nippus, J. Zabicky, G. Kimmel, Instruments & Methods in Physics Research. Section A 551 (2005) 145–151.
[19] R.E. Dinnebier, S.J.L. Billinge, Powder Diffraction Theory and Practice, RSC Publishing, Cambridge, UK, 2008.
[20] O. Glatter, O. Kratky, Small Angle X-ray Scattering, Academic Press Inc., London, 1982.
[21] L.A. Feigin, D.I. Svergun, Structure Analysis by Small-angle X-ray and Neutron Scattering, Plenum Press, New York, 1987.
[22] A. Bergmann, D. Orthaber, G. Scherf, O. Glatter, Journal Applied Crystallography 33 (2000) 869–875.
[23] A. Bergmann, G. Fritz, O. Glatter, Journal Applied Crystallography 33 (2000) 1212–1216.
[24] G. Fritz, A. Bergmann, O. Glatter, Journal Chemical Physics 113 (2000) 9733–9740.
[25] J. Nalles, D. Sendor, A. Ebbers, F.M. Petrat, H. Wiggers, C. Schulz, U. Simon, Colloid Polymer Sciences 285 (2007) 729–736.
[26] J.M. Buriak, Chemical Review 102 (2002) 1271–1308.
[27] D. Kovalev, G. Polisski, M. Ben-Chorin, J. Diener, F. Koch, Journal Applied Physics 80 (1996) 5978–5983.
[28] A. Poruba, A. Fejfar, Z. Remeš, J. Špringer, M. Vaneček, J. Kočka, J. Meier, P. Torres, A. Shah, Journal Applied Physics 88 (2000) 148–160.
[29] S. Klein, F. Finger, R. Carius, T. Dylla, J. Klamfass, Journal Applied Physics 102 (1–5) (2007) 103501.
[30] S. Knief, W. von Niessen, Physical Review B 59 (1999) 12940–12946.
[31] S.M. Sze, Physics of Semiconductor Devices, vol. 1, Wiley-Interscience Publication, New York, Chichester, Brisbane, Toronto, Singapore, 1981, 47.
[32] J. Tauc, R. Grigorovici, A. Vancu, Physica Status Solidi 15 (1966) 627–635.
[33] M. Ben-Chorin, B. Averboukh, D. Kovalev, G. Polisski, F. Koch, Physical Review Letters 77 (1996) 763–766.
[34] S.G. Dorofeev, N.N. Kononov, A.A. Ischenko, R.B. Vasil'ev, M.A. Goldschtrakh, K.V. Zaitseva, V.V. Koltashev, V.G. Plotnichenko, O.V. Tikhonevich, Semiconductors 43 (2009) 1420–1427.
[35] R.A. Forman, W.R. Thurber, D.E. Aspens, SolidState Communications 14 (1974) 1007–1009.
[36] C. Delerue, G. Allan, M. Lannoo, Physical Review B 48 (1993) 11024–11036.
[37] G. Ledoux, D. Porterat, C. Reynand, F. Huisken, B. Kohn, V. Paillard, Physical Review B 62 (2000) 15942–15951.
[38] M.V. Wolkin, J. Jorne, P.M. Fauchet, G. Allan, C. Delerue, Physical Review Letters 82 (1999) 197–200.
[39] A. Puzder, A.J. Williamson, J.C. Grossman, G. Gally, Physical Review Letters 88 (1–4) (2002) 097401.
[40] Puzder A. Puzder, A.J. Williamson, J.C. Grossman, G. Gally, Journal American Chemical Society 125 (2003) 2786–2791.
[41] C. Bulutay, S. Ossicini, in: L. Pavesi, R. Turan (Eds.), Silicon Nanocrystals: Fundamentals, Synthesis and Applications, WILEY-VCH Verlag GmbH & Co. KGaA, Weinheim, 2010, pp. 5–41.
[42] Y.J. Chabal, K. Raghavachari, X. Zhang, E. Garfunkel, Physical Review B 66 (1–4) (2002) 16135.
[43] J.S. Bitten, N.S. Lewis, H.A. Atwater, A. Polman, Applied Physics Letters 84 (2004) 5389–5391.
[44] L. Khriachtchev, M. Rasanen, S. Novikov, L. Pavesi, Applied Physics Letters 85 (2004) 1511–1513.
[45] J. Choi, S.N. Wang, V. Reipa, Langmuir 23 (2007) 3388–3394.
[46] S.T.H. Silalahi, H.Y. Yang, K. Pita, Y. Mingbin, Electrochemical Solid-State Letters 12 (2009) K29–K32.